



HST*/COS Observations of Quasar Outflows in the 500–1050 Å Rest Frame. V. Richness of Physical Diagnostics and Ionization Potential-dependent Velocity Shift in PKS J0352-0711

Timothy R. Miller¹ , Nahum Arav¹ , Xinfeng Xu¹ , Gerard A. Kriss² , and Rachel J. Plesha²

¹Department of Physics, Virginia Polytechnic Institute and State University, Blacksburg, VA 24061, USA

²Space Telescope Science Institute, 3700 San Martin Drive, Baltimore, MD 21218, USA

Received 2019 June 27; revised 2019 August 27; accepted 2019 September 2; published 2020 March 16

Abstract

We analyze absorption troughs from two outflows within PKS J0352-0711 (S1 at -1950 km s^{-1} and S2 at -3150 km s^{-1}) from spectra taken with *Hubble Space Telescope*/Cosmic Origins Spectrograph, which cover the diagnostic-rich 585–900 Å rest-frame wavelength range. In S2, for the first time we clearly detect absorption troughs from Ca IV, Ca V, Ca V*, Ca VII*, and Ca VIII*. The column density measurement of Ca V suggests S2 has a super-solar metallicity. Both outflows require at least two ionization phases where the column density of the very high-ionization phase is roughly 15 times larger than the corresponding high-ionization phase. These high column densities and very high-ionization potential ions are similar to X-ray warm absorbers. The two phases of S2 show a unique velocity centroid shift between associated troughs. Through Monte Carlo measurements of the O V* absorption troughs, we determine the electron number density of S2 (fully corroborated by independent measurements from the Ca VII* and Ca VIII* troughs), yielding a distance of 9 pc and a kinetic luminosity of $2 \times 10^{43} \text{ erg s}^{-1}$. S1 is located farther away at 500 pc from the central source with a kinetic luminosity of $10^{43} \text{ erg s}^{-1}$.

Unified Astronomy Thesaurus concepts: Active galactic nuclei (16); Active galaxies (17); Broad-absorption line quasar (183); Quasar absorption line spectroscopy (1317); Quasars (1319); AGN host galaxies (2017)

1. Introduction

Quasar outflow systems are typically identified from blue-shifted absorption troughs observed in the rest frame of quasar spectra. These outflows are found in 20%–40% of the quasar population (e.g., Hewett & Foltz 2003; Dai et al. 2008; Ganguly & Brotherton 2008; Knigge et al. 2008). The distance these outflows are from the central source (R) can be inferred from simultaneously determining the electron number density (n_e) and ionization parameter (U_H) of the outflow (e.g., Arav et al. 2013). To date, around 20 such distances have been published by our group and others using this method (see Section 1 of Arav et al. 2020, hereafter Paper I, and references therein). These distances are in the range of parsecs to tens of kiloparsecs, orders of magnitude more distant than accretion disk wind models predict (~ 0.03 pc; e.g., Murray et al. 1995; Proga et al. 2000; Proga & Kallman 2004).

Calculating the electron number density for an outflow typically requires observing troughs from excited and resonant state transitions from the same ion. Arav et al. (2013) and Finn et al. (2014) had success in determining R from spectra within the 500–1050 Å rest-frame wavelength range (EUV500) since numerous excited and resonant state transitions reside in this range. The data presented here is from a spectroscopic survey of 10 quasars with known outflows (redshifts around 1) taken during Cycle 24 aimed at probing the EUV500.

Arav et al. (2013) listed dozens of transitions within the EUV500 from very high-ionization potential ions that are typical of species seen in X-ray warm absorbers (e.g.,

Reynolds 1997; Kaastra et al. 2000; Crenshaw et al. 2003; Kaastra et al. 2014). These very high-ionization potential ions provide a link between X-ray warm absorbers and ultraviolet (UV) active galactic nucleus (AGN) outflows (Arav et al. 2013). Many of these absorption lines have yet to be detected. In this paper, we will show clear detections for some of these previously undetected absorption lines (including Ca IV–V, Ca V*, and Ca VII*–VIII*) in addition to lines from very high-ionization potential ions.

This paper is part of a series of publications describing the results of *Hubble Space Telescope* (HST) program GO-14777.

Paper I summarizes the results for the individual objects and discusses their importance to various aspects of quasar outflow research.

Paper II (Xu et al. 2020a) gives the full analysis for four outflows detected in SDSS J1042+1646, including the largest kinetic luminosity ($10^{47} \text{ erg s}^{-1}$) outflow measured to date at $R = 800$ pc and another outflow at $R = 15$ pc.

Paper III (Miller et al. 2020) analyzes four outflows detected in 2MASS J1051+1247, which show remarkable similarities, are situated at $R \sim 200$ pc, and have a combined $\dot{E}_k = 10^{46} \text{ erg s}^{-1}$.

Paper IV (Xu et al. 2020b) presents the largest velocity shift and acceleration measured to date in a broad absorption line (BAL) outflow.

Paper V is this work.

Paper VI (Xu et al. 2020c) analyzes two outflows detected in SDSS J0755+2306, including one at $R = 1600$ pc with $\dot{E}_k = 10^{46} - 10^{47} \text{ erg s}^{-1}$.

Paper VII (T. R. Miller et al. 2020, in preparation) discusses the other objects observed by program GO-14777, whose outflow characteristics make the analysis results more challenging.

* Based on observations with the NASA/ESA *Hubble Space Telescope* obtained at the Space Telescope Science Institute, which is operated by the Association of Universities for Research in Astronomy, Incorporated, under NASA contract NAS5-26555.

Table 1
HST/COS Observations from 2017 August 5 for PKS J0352-0711

<i>HST</i> /COS grating	G130M	G160M
Exposure time (s)	4072	4664
Observed range (Å)	1150–1445	1400–1780
Rest-frame range (Å)	585–735	710–905

The structure of this paper is as follows. Section 2 presents the *HST*/Cosmic Origins Spectrograph (COS; Green et al. 2012) observations of PKS J0352-0711, which cover the diagnostic-rich wavelength range blue-ward of the Lyman limit for this quasar. Section 2 also discusses the spectral fitting for the continuum and emission lines. Section 3 contrasts the amount of information contained within the EUV500 and the majority of ground-based observations with $\lambda > 1050$ Å (rest frame). Section 4 details the extraction of the ionic column densities, photoionization modeling, and electron number density determinations. Our results and discussions on the physical properties, distances, and energetics of each outflow are in Sections 5 and 6, respectively. A summary with conclusions is in Section 7. We adopt an $h = 0.696$, $\Omega_m = 0.286$, and $\Omega_\Lambda = 0.714$ cosmology throughout this paper and use Ned Wright’s Javascript Cosmology Calculator website (Wright 2006).

2. Observations, Data Reduction, and Spectral Fitting

PKS J0352-0711 ($z = 0.9662$, J2000: R.A. = 03:52:30.55, decl. = −07:11:02.3) was observed by *HST*/COS in August of 2017 (PID 14777). Table 1 contains the details of each observation. The data were processed in the same way as described in Miller et al. (2018) and corrected for Galactic extinction with $E(B-V) = 0.0686$ (Schlafly & Finkbeiner 2011). The bottom four panels of Figure 1 show the dereddened, one-dimensional spectrum in black and errors in gray. Absorption troughs for the two outflow systems are delineated with S2 and S1 for $v = -3150$ km s $^{-1}$ and $v = -1950$ km s $^{-1}$, respectively. We use the scheme of Paper I to classify each outflow. The widest absorption troughs for each outflow are from Ne VIII 770.41 Å and 780.32 Å with widths of ~ 500 km s $^{-1}$ (S1) and ~ 1400 km s $^{-1}$ (S2), classifying both outflows as mini-BALs. S2 contains the absorption troughs that have been previously undetected: O III* 599.59 Å, Ca IV 656.00 Å, Ca V 637.92 Å and 646.53 Å, Ca V* 651.53 Å, Ca VII* 630.54 Å and 639.15 Å, and Ca VIII* 596.94 Å. Intervening H absorption systems are also identified with slanted, dark green shaded regions.

In fitting the unabsorbed emission model following the methodology of Miller et al. (2018), it became apparent that the continuum emission was ill-fitted with a power law. Therefore, a cubic spline was used instead. Line emission features were modeled with Gaussian profiles. The Gaussian fits were constrained by the red side of each line since most absorption occurs on the blue side of any given emission line. Each emission line had the Gaussian centroid fixed at the rest-frame wavelength. The adopted, unabsorbed emission model is shown in Figure 1 as a solid red contour.

3. Contrasting the Analysis Potential of the EUV500 and $\lambda > 1050$ Å

The top panel of Figure 1 shows a portion of the 1993 spectra taken of PKS J0352-0711 by the Faint Object

Spectrograph (FOS) aboard *HST* and reported in the *HST*/FOS Spectral Atlas by Bechtold et al. (2002). This spectra covers the rest-frame wavelength range of 1130–1665 Å and covers much of the useful $\lambda > 1050$ Å rest-frame region observed in high-ionization outflows. The majority of ground-based observations show only the absorption troughs seen in the figure for high-ionization outflows. They are usually saturated (e.g., Borguet et al. 2012b), resulting in lower limits to their ionic column densities. Of the troughs shown for S2, the Si IV troughs yield an ionic column density (N_{ion}) measurement while the rest give lower limits. Only lower bounds to the hydrogen column density (N_{H}) and U_{H} can be found with such limited data. These troughs are all from resonance transitions, making n_e determinations (needed to calculate R and the energetics) impossible. Therefore, limited insight into the physical parameters and geometry of S2 can be obtained from such data. There is only a hint that S1 exists with the N V 1242.80 Å trough.

In contrast, the EUV500 data contains troughs from not only high-ionization potential ions (e.g., O III, O IV, and N III) like those present in the FOS data but also very high-ionization potential ions (e.g., Mg X, Na IX, and Ne VIII). Such ions have ionization potentials typical of X-ray warm absorbers observed in nearby Seyfert galaxies. Several troughs will be shown to yield N_{ion} measurements, constraining U_{H} and N_{H} . There are numerous troughs from excited state transitions, yielding measurements or constraints on n_e for an outflow. Thus, the distance and energetics can be determined, yielding a full physical picture of the outflows as well as the potential for AGN feedback. This is made possible by the higher density of observable transitions in the EUV500, resulting in a factor of six increase in detected troughs (from 8 to about 50) over a similar $\Delta\lambda/\lambda$ covered by the FOS and COS observations.

4. Data Analysis

4.1. Ionic Column Density Measurements

The column density for a particular ion was measured using two methods: (1) the apparent optical depth (AOD) method, and (2) the partial covering (PC) method (e.g., Miller et al. 2018). Therefore, a single N_{ion} for a given ionic energy state is determined by one ionic transition (AOD method) or two ionic transitions (PC method). The PC method yields reliable results when multiple lines from the same ionic energy state and different oscillator strengths have different trough depths, allowing for the measurement of a viable PC solution. Table 2 lists the total (sum of all observed ionic energy states) column density for each ion in both outflow systems. The ratio of the measured column densities to the predicted column densities from the best-fit model are also given (see Section 4.2 and Figure 3). When the measured N_{ion} are lower limits, we expect this ratio to be less than one and vice versa for upper limits. Many excited states have multiple transitions with small wavelength separations (< 0.5 Å). In such cases, we combine each set of transitions into a single transition for labeling in Figure 1. A list of atomic data for the transitions can be found in Table 3 of Paper II.

Non-black saturation is a concern, so we use the scheme used in Paper II to decide on ionic column density measurements, lower limits, and upper limits: PC N_{ion} are measurements, regions where the maximum optical depth, τ_{max} , is less than 0.05 are taken as upper limits; troughs that have

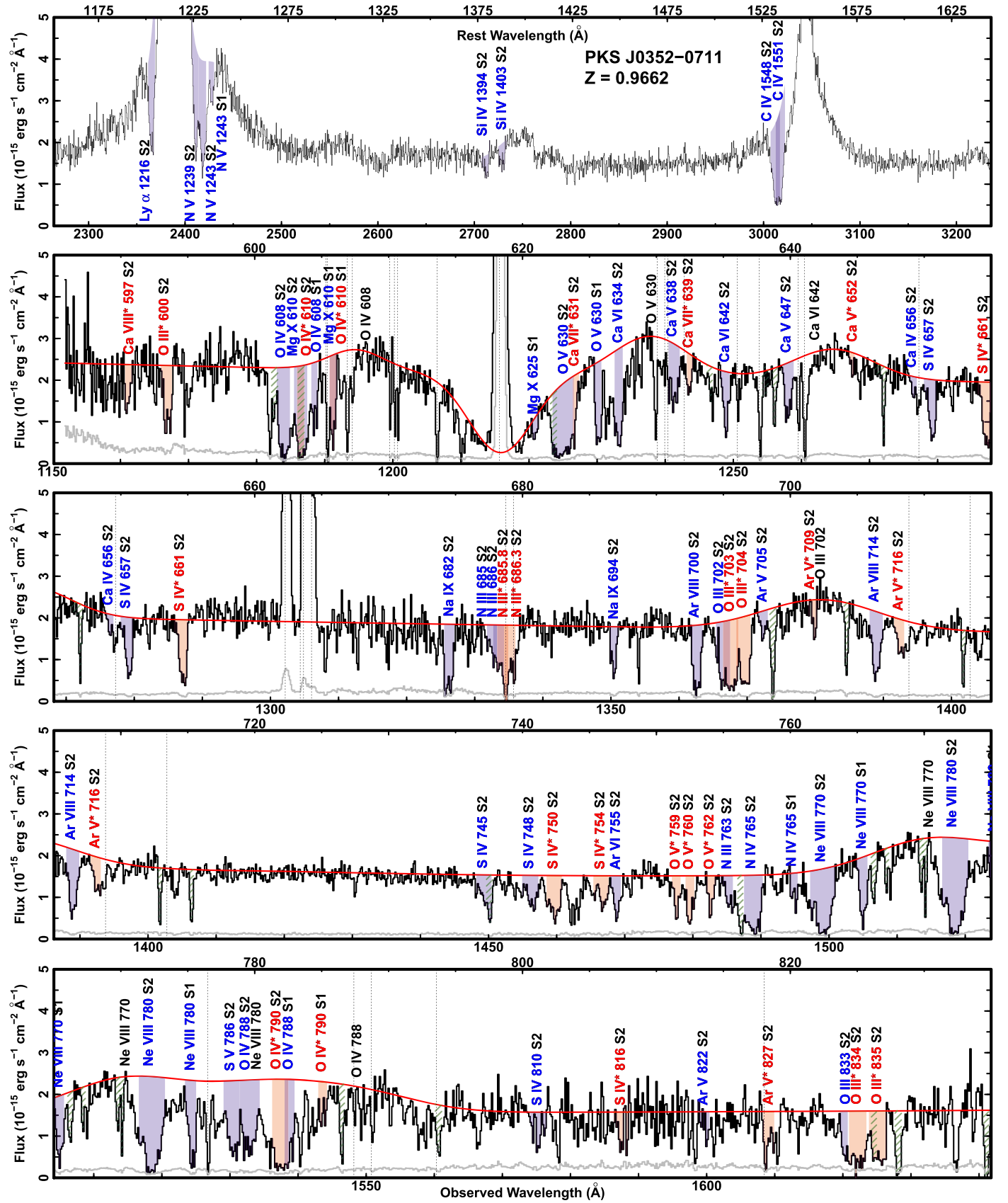


Figure 1. On top is a portion of the 1993 *HST*/FOS spectrum in black with troughs labeled and marked with blue shaded regions from the -3150 km s $^{-1}$ (S2) and -1950 km s $^{-1}$ (S1) outflows. The rest is a portion of the dereddened, 2017 *HST*/COS spectrum (in black) with errors (in gray). The main absorption troughs are labeled for S2 and S1. Blue shaded regions mark transitions from resonance absorption lines and red are for excited ones. Absorption troughs from intervening systems are the slanted, dark green shaded regions and the vertical dashed lines mark Galactic absorption and geocoronal emission features. The red contour traces the unabsorbed emission model. Emission lines are labeled in black.

Table 2
Total Ionic Column Densities

Ion	AOD (10^{12}cm^{-2})	PC (10^{12}cm^{-2})	Adopted (10^{12}cm^{-2})	Adopted Best Model
$v = -3150 \text{ km s}^{-1}$				
N III	890^{+170}_{-150}	...	>890 –230	$>0.39_{-0.17}$
N IV	610^{+50}_{-30}	...	>610 –130	$>0.02_{-0.01}$
O III	7700^{+450}_{-260}	...	>7700 –1600	$>1.90_{-0.74}$
O IV	13000^{+810}_{-500}	...	>13000 –2700	$>0.10_{-0.04}$
O V	4600^{+590}_{-260}	...	>4600 –940	$>0.02_{-0.01}$
Ne VIII	15000^{+850}_{-460}	...	>15000 –3000	$>0.07_{-0.03}$
Na IX	2000^{+210}_{-190}	2700^{+960}_{-340}	2700^{+1100}_{-650}	$2.11^{+2.28}_{-0.86}$
S III	60^{+10}_{-10}	...	$<60^{+20}$	$<0.30^{+0.31}$
S IV	340^{+20}_{-10}	...	>340 –70	$>0.11_{-0.04}$
S IV	1600^{+250}_{-170}	...	$<1600^{+410}$	$<0.50^{+0.52}$
S V	160^{+10}_{-10}	...	>160 –30	$>0.03_{-0.01}$
Cl V	100^{+30}_{-20}	...	$<100^{+40}$	$<0.28^{+0.30}$
Cl VII	220^{+30}_{-20}	...	$<220^{+50}$	$<0.47^{+0.48}$
K V	210^{+70}_{-70}	...	$<210^{+80}$	$<1.96^{+2.15}$
K VI	1000^{+230}_{-170}	...	$<1000^{+310}$	$<2.79^{+2.89}$
K VII	250^{+70}_{-70}	...	$<250^{+90}$	$<0.35^{+0.37}$
K IX	200^{+40}_{-30}	...	$<200^{+60}$	$<0.59^{+0.62}$
Ar IV	880^{+260}_{-210}	...	$<880^{+310}$	$<1.46^{+1.56}$
Ar V	1100^{+140}_{-110}	...	$<1100^{+270}$	$<0.28^{+0.29}$
Ar VI	1500^{+170}_{-70}	...	>1500 –290	$>0.30_{-0.12}$
Ar VIII	930^{+50}_{-40}	1400^{+290}_{-140}	1400^{+390}_{-330}	$0.15^{+0.16}_{-0.06}$
Ca IV	1100^{+290}_{-190}	...	>1100 –280	$>2.62_{-1.15}$
Ca V	9100^{+550}_{-590}	...	>9100 –1900	$>4.52_{-1.78}$
Ca VI	2500^{+170}_{-230}	...	>2500 –670	$>0.39_{-0.16}$
Ca VII	1500^{+120}_{-180}	...	>1500 –370	$>0.06_{-0.02}$
Ca VIII	1400^{+280}_{-180}	...	>1400 –330	$>0.06_{-0.03}$
Mg X	6700^{+500}_{-350}	...	>6900 –1400	$>0.41_{-0.16}$
$v = -1950 \text{ km s}^{-1}$				
N III	80^{+30}_{-30}	...	$<80^{+40}$	$<4.53^{+4.60}$
N IV	130^{+30}_{-20}	...	>130 –30	$>0.25_{-0.12}$
O IV	1500^{+260}_{-150}	1700^{+290}_{-190}	1700^{+450}_{-380}	$1.08^{+1.12}_{-0.43}$
O V	410^{+20}_{-20}	...	>410 –160	$>0.05_{-0.02}$
Ne VIII	4000^{+290}_{-190}	...	>4000 –810	$>0.35_{-0.14}$
Na IX	140^{+70}_{-70}	...	$<140^{+80}$	$<1.28^{+1.28}$
Mg X	1500^{+220}_{-260}	1700^{+100}_{-190}	1700^{+330}_{-400}	$0.95^{+0.97}_{-0.38}$
S IV	7^{+2}_{-3}	...	$<7^{+2}$	$<0.73^{+0.77}$
Ar VI	90^{+50}_{-50}	...	$<90^{+60}$	$<0.83^{+1.01}$
Ar VIII	80^{+20}_{-20}	...	$<80^{+30}$	$<1.07^{+1.20}$
Ca VII	320^{+120}_{-140}	...	$<320^{+130}$	$<0.99^{+1.08}$

Note. Total ionic column densities (excited plus resonance, where applicable) for each outflow system with the measured and adopted values and errors. Adopted values in bold are lower limits, upper limits are in italics, and measurements are in roman. The ratio of the adopted values to the column densities from the best-fit Cloudy model are in the last column, and those errors also account for the uncertainty in metallicity of each element.

$0.05 < \tau_{\text{max}} < 0.5$ with other troughs from similar ionization potential ions that have $\tau_{\text{max}} > 2$ are also taken as measurements; and all others are lower limits. We report both the upper and lower limit N_{ion} for S IV of S2. They are measured from the S IV 810 and S IV* 816 regions (upper limit) and the S IV 657 and S IV* 661 troughs (lower limit). The S IV troughs around 750 Å are blended with unknown absorption, yielding unreliable PC N_{ion} . Following previous works (e.g., Miller et al. 2018;

Table 3
 $Z = 4.68 Z_{\odot}$ Composition

Element	X/H	X/X_{\odot}
C	$(5.4 \pm 2.70) \times 10^{-4}$	2.00 ± 1.00
N	$(5.0 \pm 2.50) \times 10^{-4}$	7.41 ± 3.71
O	$(1.5 \pm 0.75) \times 10^{-3}$	3.02 ± 1.51
Ne	$(3.4 \pm 1.70) \times 10^{-4}$	4.00 ± 2.00
Na	$(6.9 \pm 3.45) \times 10^{-6}$	4.00 ± 2.00
Mg	$(2.0 \pm 1.00) \times 10^{-4}$	4.90 ± 2.45
Al	$(1.2 \pm 0.60) \times 10^{-5}$	4.00 ± 2.00
Si	$(4.4 \pm 2.20) \times 10^{-4}$	13.49 ± 6.75
P	$(1.0 \pm 0.50) \times 10^{-6}$	4.00 ± 2.00
S	$(1.3 \pm 0.65) \times 10^{-4}$	10.00 ± 5.00
Cl	$(3.2 \pm 1.60) \times 10^{-6}$	10.00 ± 5.00
Ar	$(2.5 \pm 1.25) \times 10^{-5}$	10.00 ± 5.00
K	$(1.1 \pm 0.55) \times 10^{-6}$	10.00 ± 5.00
Ca	$(2.5 \pm 1.25) \times 10^{-5}$	11.48 ± 5.74
Fe	$(3.7 \pm 1.85) \times 10^{-4}$	11.74 ± 5.87

Note. Elements in bold are from Ballero et al. (2008).

Xu et al. 2018), the adopted value is chosen to be the PC N_{ion} when available, or else it is the AOD N_{ion} limits. To account for systematics in the unabsorbed emission model, all adopted error values (see Table 2) have added an additional 20% error in quadrature (e.g., Miller et al. 2018; Xu et al. 2018).

4.2. Photoionization Modeling

Given that the troughs of each outflow are narrow and any blended troughs do not hinder our analysis, we follow the methodology of previous works (e.g., Miller et al. 2018; Xu et al. 2018, 2019) and not the Synthetic Spectral Simulation (SSS) method in Paper II. To determine the N_{H} and U_{H} that best model the outflow system, a grid of Cloudy (Ferland et al. 2017, version c17.00) photoionization models were generated. We used two metallicities and three spectral energy distributions (SEDs): the UV-soft SED (Dunn et al. 2010), the HE0238 SED (Arav et al. 2013), and the MF87 SED (Mathews & Ferland 1987). These three SEDs were chosen since they give a representative range of SED shapes that are commonly attributed to radio quiet quasars (Arav et al. 2013), .

The two metallicities are solar (Z_{\odot} , Grevesse et al. 2010) and super-solar ($Z = 4.68 Z_{\odot}$, see Table 3). These were chosen since chemical abundances of outflow systems have been shown to be between solar and 4–5 times solar (e.g., Gabel et al. 2006; Arav et al. 2007, 2020). The super-solar abundances for C, N, O, Mg, Si, Ca, and Fe are from Table 2 of Ballero et al. (2008) for the $10^{11} M_{\odot}$ bulge mass. We note that their quoted metallicity ($7.22 Z_{\odot}$) is likely in error as we calculate $4.1 Z_{\odot}$ assuming all other elements remain solar and 4.68 with the enhancement of all other elements described next. The abundances of the other elements were chosen to be increased above solar by a factor similar to the elements from Ballero et al. (2008) that come from the same fusion sources (i.e., Ne–Al and P have sources of C and Ne, while Si and S–Ca have sources of O and Si; e.g., Anders & Grevesse 1989; Arnett 1996) instead of a simple linear increase with Z (e.g., Hamann & Ferland 1993). Since we are uncertain of both the super-solar abundances from Ballero et al. (2008) given the metallicity discrepancy and our values for the other elements, we assume an abundance uncertainty in each element of 50%. This uncertainty is based on the relative error between the

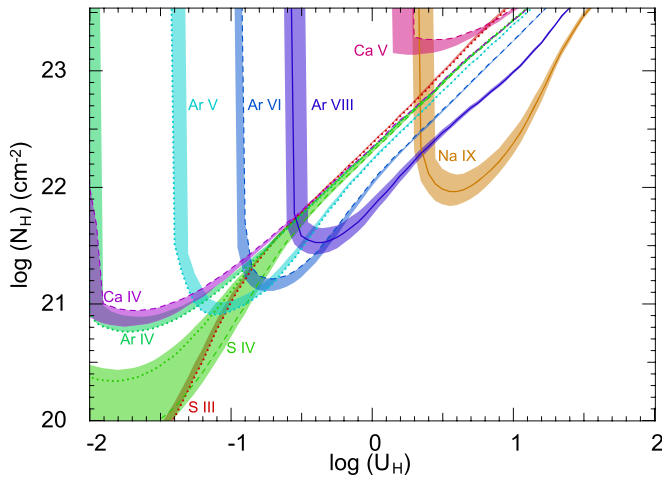


Figure 2. Colored contours show the model parameters that are consistent with the observed values assuming the HE0238 SED and solar metallicity. Solid contours represent ionic column densities taken as measurements, and dotted or dashed contours represent N_{ion} upper or lower limits, respectively. The shaded bands are the 1σ uncertainties for each contour (see Table 2). For clarity’s sake, only a subset of all ions are shown. Any solution that matches the lower limit column density of Ca V overpredicts the column densities of Ar IV, Ar V, Ar VIII, and S IV by up to a factor of 10. Invoking a super-solar metallicity is a possible solution.

metallicity given by Ballero et al. (2008) and what we determine, i.e., $(7.22-4.68)/4.68 \approx 50\%$.

For a particular pair of N_{H} and U_{H} , ionic column densities from the model are compared to the measured counterparts. In Figure 2, the colored contours for individual ions show where each model-predicted N_{ion} , assuming the HE0238 SED and solar metallicity, is consistent ($<1\sigma$) with the corresponding observed values for S2. The colored contours with solid lines are ionic column densities treated as measurements and dotted or dashed lines are N_{ion} upper or lower limits, respectively. It is evident that for solar metallicity, there is no viable solution. Any solution that matches the lower limit column density of Ca V will simultaneously overpredict the column densities of Ar IV, Ar V, Ar VIII, and S IV by up to two orders of magnitude. The same is true for the other two SEDs. One possible solution is to invoke a super-solar metallicity to reduce the N_{H} required to match the observations of Ca V.

Figure 3 shows the same contours for both S1 and S2, assuming the HE0238 SED but with $Z = 4.68 Z_{\odot}$. The best-fit solution is determined through χ^2 -minimization of the model-predicted N_{ion} compared to the measured ionic column densities (all values in Table 2 when accounting for the uncertainty in the metallicity). The solutions and corresponding 1σ uncertainties are the black dots and ellipses. However, for S2, we also take into account that the O V^* column density primarily comes from the very high-ionization phase (see Section 5.2), which shifts the solution to the red dots and constrains the errors to the red ellipses (the overlap of the 1σ contours for O V^* and the black ellipses). Imposing the same O V^* constraint and using the other SEDs yields no overlap between the 1σ contours for O V^* and the black ellipses, i.e., a worse solution for the very high-ionization phase. Therefore, the adopted best-fit solutions for S1 and S2 are those with the HE0238 SED and super-solar metallicity since we assume both outflows have the same incident SED and metallicity. Both outflow systems require a two-phase photoionization solution to satisfy the column densities from both the very high-ionization

potential ions and high-ionization potential ions (see Arav et al. 2013). A single phase solution at the intersection of the O IV and Mg X contours for S1 overpredicts the upper limit column density of Ar VI by over a factor of five. Similarly, the very high-phase solution of S2 produces negligible amounts of the S IV column density, and the high-phase solution fails to reproduce the observed column density of Na IX, necessitating a two-phase solution. However, even this two-phase solution under predicts the column density of Ca V by almost a factor of five ($<2\sigma$) and overpredicts the column density of S III by a factor of three ($\approx 2\sigma$) and the column density of Ar VIII by nearly a factor of seven ($\approx 5\sigma$). However, the discrepancy with Ar VIII depends on our estimate for the abundance of Ar VIII, of which an enhancement of only twice solar would reduce the difference to within 2σ .

4.3. Determining n_e

All of the excited state troughs shown in Figure 1 become populated through collisions with free electrons. These collisions depend on both the electron number density and gas temperature. Therefore, calculating the relative populations between an excited and resonance or two excited states will yield n_e (e.g., de Kool et al. 2001, 2002; Hamann et al. 2001; Korista et al. 2008). Following the methodology of previous works (e.g., Borguet et al. 2012b; Arav et al. 2013, 2015, 2018; Chamberlain & Arav 2015), we used the CHIANTI 8.0.7 database (Dere et al. 1997; Landi et al. 2013) to calculate the predicted population ratios from the states of each ion. This ratio is equal to the ratio of the measured N_{ion} .

However, not all of the observed excited states are useful for this approach. Ca VII* 630.54 Å is blended with O V 629.73 Å. N III* 685.82 Å and 686.34 Å are heavily blended with not only each other and N III 685.52 Å, but also with Galactic absorption from C II 1334.53 Å and C II* 1335.71 Å. Comparing troughs from the same energy level for a particular ion, Ca v 637.92 Å and 646.53 Å; O III 702.34 Å and 832.93 Å; O IV 608.40 Å and 787.71 Å; O III* 702.90 Å, 703.85 Å, 833.75 Å, and 835.29 Å; and O IV* 609.83 Å and 790.20 Å of the S2 outflow system exhibit 1:1 trough depths. The PC method is unusable in these instances since the troughs are saturated and the PC method needs at least one trough from a given ionic energy state to be shallower. This leaves O V* 759.44 Å, 760.45 Å, and 762.00 Å; S IV* 661.40 Å, 750.22 Å, and 753.76 Å (with S IV 657.32 Å, 744.90 Å, and 748.39 Å); Ca VIII* 596.94 Å; and Ca VII* 639.15 Å as potentially useful density diagnostics for S2 and O IV* 790.20 Å (with O IV 608.40 Å and 787.71 Å) for S1.

For O V*, the line at 759.44 Å is from the $J = 0$ ($81,942 \text{ cm}^{-1}$) energy level and the other two lines are from the $J = 2$ ($82,385 \text{ cm}^{-1}$) energy level (for additional lines and transition parameters, see Paper II). Therefore, using the $J = 2$ lines with the PC method yields one column density, and assuming the same covering solution, the column density for the $J = 0$ energy level and subsequent ratio can be calculated. We assume the temperature of the very high-ionization phase (52,700 K) for reasons discussed in Section 5.2. However, given the signal-to-noise ratio of the data, directly measuring the ionic column density from the data yielded a ratio with large enough errors that only a lower limit on n_e could be determined, i.e., the ratio is consistent with the theoretical Boltzmann limit (≈ 5 in the top panel of Figure 6). To obtain a better constrained n_e , we fit each of the absorption troughs

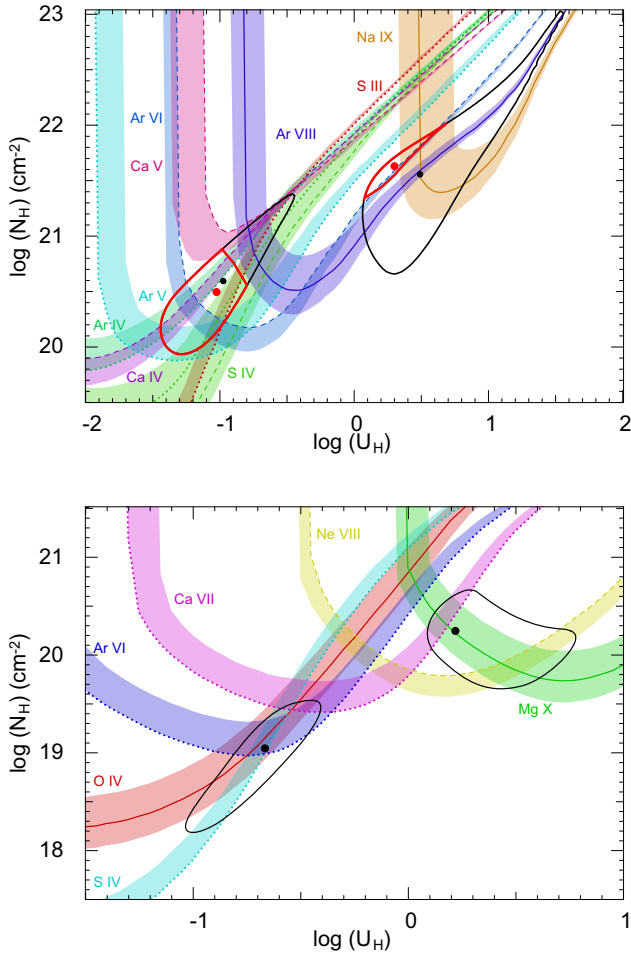


Figure 3. Colored contours show the model parameters that are consistent with the observed values assuming the HE0238 SED and $Z = 4.68 Z_{\odot}$ (see Table 3). For clarity's sake, only a subset of all ions are shown. Solid contours represent N_{ion} measurements, while dotted and dashed contours are N_{ion} upper and lower limits, respectively. The shaded bands are the 1σ uncertainties for each contour, including the uncertainty in the metallicity (see Tables 2 and 3). Top: two-phase photoionization solution for the S2 outflow system. The black dots are the χ^2 -minimization solutions for each ionization phase based on the total ionic column densities, and the ellipses encircling them are their 1σ uncertainties. The red dots and corresponding ellipses take into account the O V^* column density constraint and are chosen as the best solution (see Section 4.2). Bottom: two-phase photoionization solution for the S1 outflow system. The black dots are the best χ^2 -minimization solutions for each ionization phase, and the ellipses encircling them are their 1σ uncertainties.

using Gaussian optical depth profiles over the velocity range -3300 – -3000 km s^{-1} (See Figure 4):

$$\tau_i(v) = \frac{A_i}{\sigma_i \sqrt{2\pi}} * \exp\left(-\frac{(v - v_i)^2}{2\sigma_i^2}\right), \quad (1)$$

$$I_i(v) = \exp(-\tau_i), \quad (2)$$

where for trough i , A_i is scaling factor, σ_i is the velocity dispersion ($\text{FWHM} = 2\sqrt{2\ln(2)}\sigma$), v_i is the velocity centroid, and $I_i(v)$ are the fitted, normalized flux values. The fitting parameters for each trough were allowed to vary independent of each other, resulting in nine parameters with associated errors (See Table 4). The same PC procedure outlined above can then be used on these fitted functions to get the ratio. To propagate errors, we used a Monte Carlo approach, randomly

choosing each parameter from a normal distribution 10,000 times and calculating the final ratio. The distribution of the ratios is shown in Figure 5, and we adopt $\frac{N(J=2)}{N(J=0)} = 3.4^{+1.1}_{-0.9}$.

In the top panel of Figure 6, the red contour shows the expected column density ratio as a function of electron number density for O V^* as determined by CHIANTI for a temperature of 52,700 K, which is determined by the Cloudy solution for the very high phase. Overlaid on that contour is the measured column density ratio and uncertainties from the Monte Carlo results. We calculate an O V^* derived n_e for the very high-ionization phase of S2 to be $\log(n_e) = 5.8^{+0.5}_{-0.3} \text{ cm}^{-3}$. Since the velocity centroids of the troughs from the high- and very high-ionization phase solutions of S2 are similar, it is very likely that they are at the same distance. For the two phases to be located at the same distance, the high phase must have an n_e larger by a factor equal to the ratio of the two ionization parameters (see Equation (3)): $\log(n_e) = 7.1^{+0.8}_{-0.4} \text{ cm}^{-3}$. The S IV^* and S IV absorption troughs are primarily produced by the high-ionization phase and yield a $\log(n_e) > 5$, which is consistent with our assumed value of 7.1.

There are two additional n_e diagnostics for S2 that can be calculated from Ca VII^* and Ca VIII^* . We first used the model-predicted values for the total N_{ion} of Ca VII and Ca VIII along with our measured N_{ion} of Ca VII^* and Ca VIII^* to estimate the ground state populations of each ion. This is possible since the very high-ionization phase produces over 90% of both total N_{ion} . Then we calculated the ratio of each excited state to the estimated ground state. Plotting these with their CHIANTI contours as seen in Figure 6 shows consistent values for n_e between all three diagnostics.

For the O IV and O IV^* troughs of S1, the O IV 608.40 Å and O IV^* 790.19 Å lines are not blended with any other lines, but the O IV 787.71 Å line is blended on the blue side with the O IV^* 790.19 Å line of S2 (See Figure 7). Since the O IV^* trough is shallower than the O IV 787.71 Å trough and they have the same oscillator strength value, the N_{ion} of O IV^* is less than the N_{ion} of O IV . Therefore, n_e for S1 is smaller than the critical density of $\log(n_{e,\text{crit}}) = 4.1$ for this diagnostic (see Arav et al. 2018). We assume the trough is symmetric and double the red half PC N_{ion} value for the O IV N_{ion} . We use the covering solution of the O IV 608.40 Å and 787.71 Å doublet along with the O IV^* 790.19 Å trough to determine the O IV^* ionic column density in the same way as above since the O IV^* 609.83 Å line is blended with the Mg X 609.79 Å line. O IV is produced by the high phase, of which has a gas temperature of 15,900 K as determined by the Cloudy model solution. The bottom panel of Figure 6 shows the resulting ratio, and we calculate $\log(n_e) = 3.2^{+0.2}_{-0.1} \text{ cm}^{-3}$ for the high phase. There are no density diagnostic troughs for the very high phase of S1.

5. Results

5.1. Outflow Properties, Distance, and Energetics

From the definition of the ionization parameter, we can determine the distance each outflow is from the central source:

$$U_H = \frac{Q_H}{4\pi R^2 n_H c}, \quad (3)$$

where R is the distance from the central source, n_H is the hydrogen number density ($n_e \approx 1.2n_H$ for highly ionized plasma), c is the speed of light, and Q_H is the ionizing hydrogen

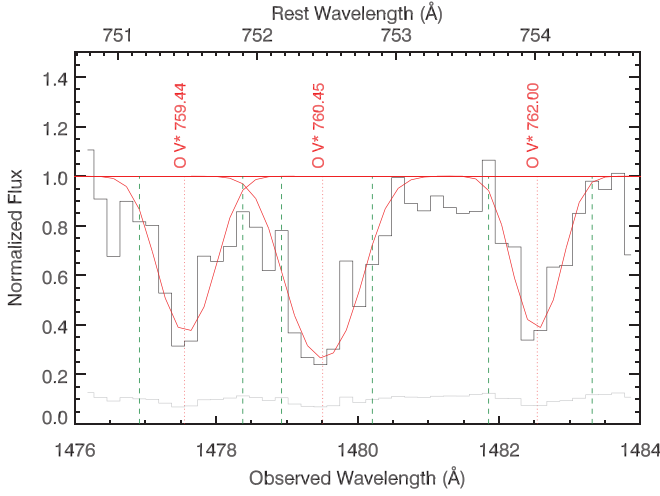


Figure 4. Best-fitting Gaussian profiles for the O V* 760.45 Å ($J=2$), 762.00 Å ($J=2$), and 759.44 Å ($J=0$) absorption troughs in red are overlaid on the data in black. The vertical red dotted lines mark the velocity centroid, and the vertical green dashed lines show the fitting range.

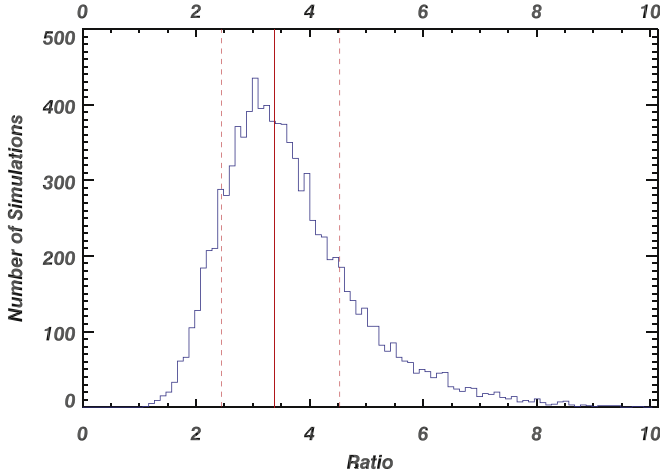


Figure 5. Monte Carlo ratio distribution for the O V* 760.45 Å ($J=2$), 762.00 Å ($J=2$), and 759.4 Å ($J=0$) absorption troughs. The solid red line is the ratio determined from the best-fitting Gaussian profiles, and the dashed red lines mark the 1σ boundaries of the distribution.

Table 4
Best-fitting Gaussian Parameters for the O V* Multiplets

Line	A_i (km s $^{-1}$)	σ_i (km s $^{-1}$)	v_i (km s $^{-1}$)
O V* 759.4	170 ± 23	68 ± 10	-3158 ± 11
O V* 760.4	280 ± 40	84 ± 15	-3162 ± 14
O V* 762	141 ± 18	59 ± 8	-3164 ± 9

photon rate. Q_H was calculated by integrating the HE0238 SED for energies above 1 Ryd, yielding $Q_H = 3.1 \times 10^{56} \text{ s}^{-1}$. Under the assumption of a partially filled, thin shell outflow presented by Borguet et al. (2012a), the mass flow rate and kinetic luminosity are given by, respectively,

$$\dot{M} \simeq 4\pi\Omega R N_H \mu m_p v \quad (4)$$

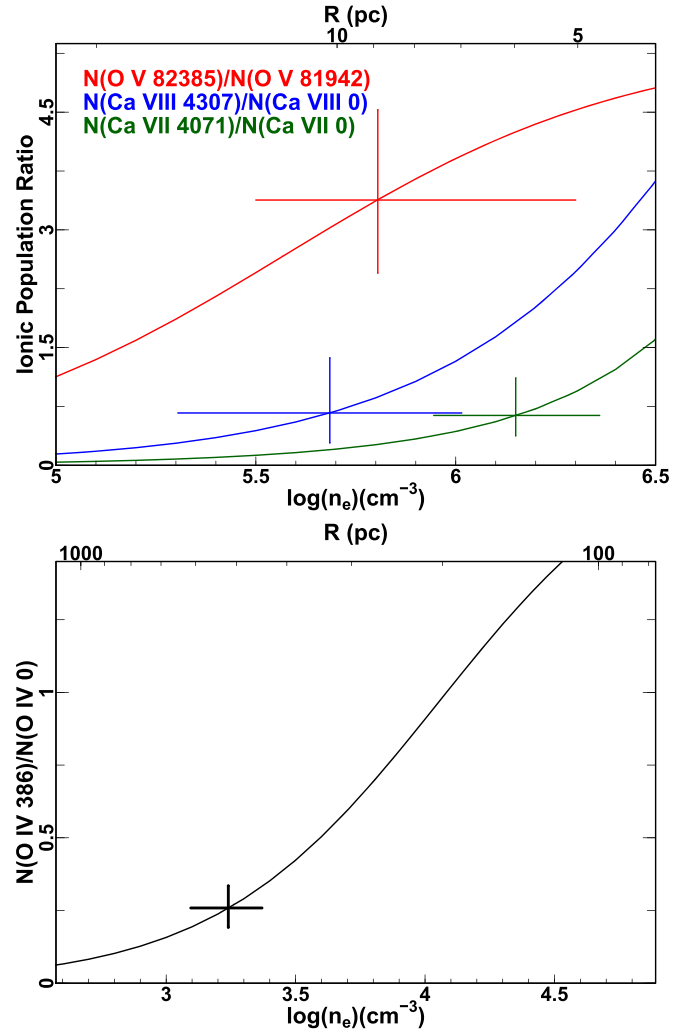


Figure 6. Top: the electron number density, n_e , and the distance from the central source, R (Equation (3)), of the S2 outflow system based on the lines of O V, Ca VII, and Ca VIII. The average temperature from the photoionization solution for the very high-ionization phase is 52,700 K. The ratios and CHIANTI contours of Ca VII and Ca VIII have been scaled up by a factor of 10 for clarity's sake. The distance on the top axis assumes the O V* n_e and U_H of the very high-phase solution. Bottom: n_e for the S1 outflow system based on the O IV ratio. The assumed temperature is 15,900 K. The distance axis assumes the U_H of the high-phase solution. See Section 4.3.

and

$$E_K \simeq \frac{1}{2} \dot{M} v^2, \quad (5)$$

where R is the distance from the central source, $\mu = 1.4$ is the mean atomic mass per proton, N_H is the hydrogen column density, m_p is the proton mass, v is the outflow velocity, and Ω is the global covering factor. Since we can not directly measure how much the outflow covers the source, we use the frequency of Ne VIII mini-BAL outflow detections as a proxy, i.e., $\Omega = 0.40^{+0.14}_{-0.14}$ (Muzahid et al. 2013). Table 5 contains the physical properties, energetics, and distances for each outflow system. As can be seen, S2 is fairly close to the central source at 8.9 pc, while S1 is much farther out at 520 pc.

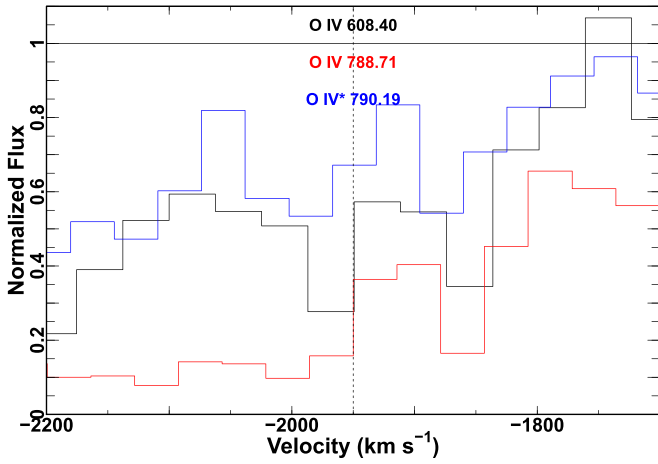


Figure 7. Overlap of the O IV 608.40 Å, O IV 788.71 Å, and O IV* 790.19 Å troughs for S1. To the left of the vertical, dotted line (-1950 km s^{-1}) is the blend of the O IV* 790.20 Å trough of S2 with the O IV 788.71 Å trough of S1. To the right of the line is not blended, allowing for the ionic column density of the resonance lines to be determined.

Table 5

Physical Properties, Distances, and Energetics of the Two Outflow Systems

Outflow System Ionization Phase	-3150 km s^{-1} (S2)		-1950 km s^{-1} (S1)	
	Very High	High	Very High	High
$\log(N_H)$ [cm^{-2}]	$21.63^{+0.27}_{-0.30}$	$20.50^{+0.38}_{-0.66}$	$20.25^{+0.42}_{-0.59}$	$19.05^{+0.49}_{-0.86}$
$\log(U_H)$ [dex]	$0.3^{+0.4}_{-0.2}$	$-1.0^{+0.2}_{-0.5}$	$0.2^{+0.6}_{-0.1}$	$-0.7^{+0.3}_{-0.3}$
$\log(n_e)$ [cm^{-3}]	$5.8^{+0.5}_{-0.3}$	$^a 7.1^{+0.8}_{-0.4}$	$^a 2.4^{+0.3}_{-0.7}$	$3.2^{+0.2}_{-0.1}$
Distance [pc]	$8.9^{+4.9}_{-4.5}$		520^{+300}_{-150}	
\dot{M} [$M_\odot \text{ yr}^{-1}$]	$7.5^{+9.0}_{-4.9}$		$11.2^{+21.8}_{-8.2}$	
$\log(\dot{E}_K)^b$ [erg s^{-1}]	$43.37^{+0.34}_{-0.46}$		$43.13^{+0.47}_{-0.57}$	
\dot{E}_K/L_{edd} [%]	$0.02^{+0.06}_{-0.01}$		$0.01^{+0.04}_{-0.01}$	
$\log(f_\nu)$	$-2.4^{+0.6}_{-0.9}$		$-2.1^{+0.8}_{-1.2}$	

Notes.

^a Assuming that both ionization components are at the same distance.

^b Assuming $\Omega = 0.37$ where N_H is the sum of the two ionization phases.

^c Bolometric luminosity, $L_{\text{bol}} = 5.5^{+0.1}_{-0.1} \times 10^{46} \text{ erg s}^{-1}$, assuming the HE0238 SED.

5.2. Velocity Centroid Offset between Troughs in S2

In analyzing the S2 absorption troughs, we noticed a velocity centroid shift between ions of different ionization potentials. To quantify this shift, we used Gaussian optical depth profiles to fit troughs where the deepest parts had normalized flux values less than 0.5. We only fitted the sections of each trough that were not heavily contaminated due to blending or intervening systems. We also restricted each trough for a particular ion to have the same velocity centroid and simultaneously fit those

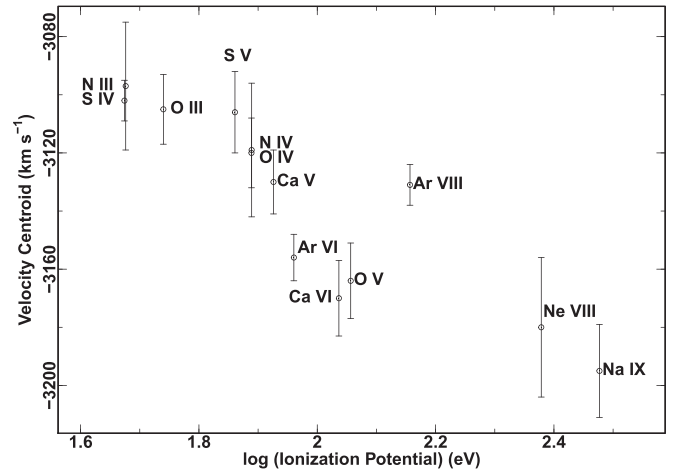


Figure 8. Velocity centroid (from Gaussian profile fits) for troughs in S2 as a function of the ionization potential of each ion. There is an increase in the magnitude of the velocity for higher ionization potential ions, suggesting that there is a velocity offset between the two photoionization solutions (see Section 5.2 and Figure 3).

troughs, minimizing the effects of spurious data or unidentified contaminations. Figure 8 shows that the fitted velocity centroid for each ion tends to increase in magnitude with an increase in ionization potential. This suggests that the two photoionization solutions are offset in velocity as the column densities of Na IX and S IV, for example, are produced entirely by the very high phase and high phase, respectively. Therefore, the O V* troughs, with their higher velocity centroids (see Table 4), should primarily be produced by the very high phase.

6. Discussion

6.1. S2 Photoionization Solution and n_e Accuracy

As shown in Section 4.3, the n_e derived from the O V*, Ca VII*, and Ca VIII* diagnostic ratios for the very high phase of S2 all gave consistent results. The photoionization solution for this phase, which yielded our estimates for the N_{ion} of Ca VII and Ca VIII, was determined primarily by the constraints imposed by the N_{ion} measurements of O V*, Na IX, and Ar VIII; and not by the Ca VII* and Ca VIII* N_{ion} lower limits. Therefore, the fact that the photoionization solution gave Ca VII and Ca VIII N_{ion} values such that the n_e derived were all within errors speaks to the accuracy and robustness of the photoionization solution and n_e .

6.2. AGN Feedback Contribution

To judge the potential for AGN feedback, kinetic luminosities exceeding 0.5% Hopkins & Elvis (2010), or 5% Scannapieco & Oh (2004), of the Eddington luminosity are thought to be sufficient. Using the Mg II-based equation from Bahk et al. (2019) and their methodology for measuring the Mg II emission line FWHM and local continuum level from Sloan Digital Sky Survey (SDSS) data, we estimate the mass of the super massive black hole to be $8.7^{+11.8}_{-5.6} \times 10^8 M_\odot$ (including systematics). This corresponds to an Eddington luminosity (L_{edd}) of $1.1^{+1.5}_{-0.7} \times 10^{47} \text{ erg s}^{-1}$. Taking the ratio of the kinetic luminosities with respect to L_{edd} gives 0.02% and 0.01% for S2 and S1, respectively (see Table 5). Therefore, these outflows in PKS J0352-0711 are not significant contributors to AGN feedback processes.

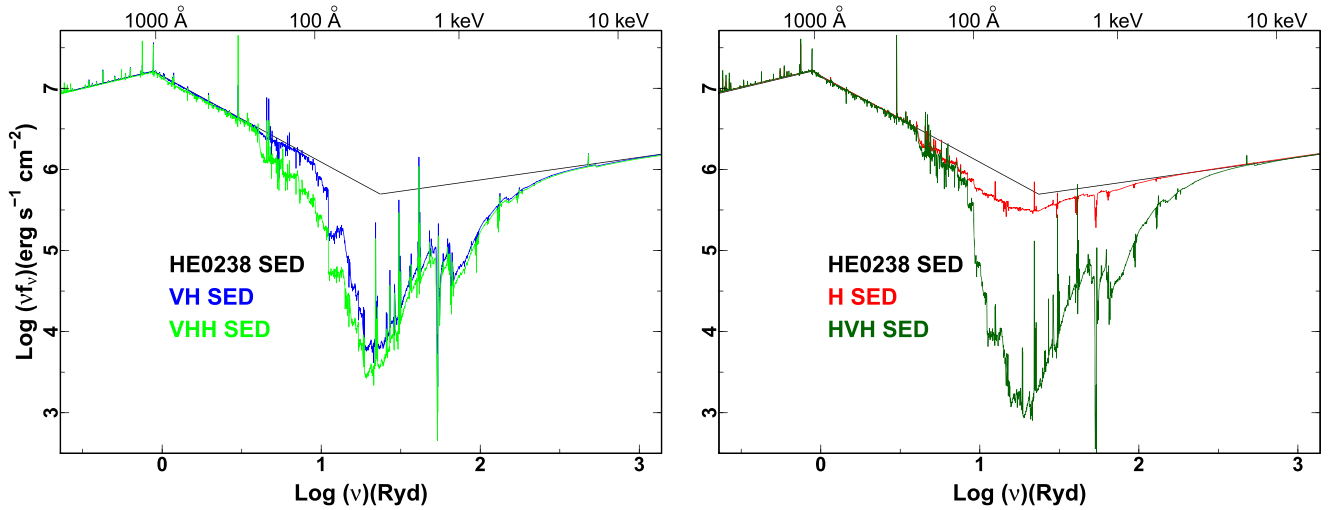


Figure 9. Comparison between the HE0238 SED and the transmitted SEDs. The attenuations are similar in shape but stronger in absorption to what is seen in Paper II. Left panel: the VH SED (in blue) is the transmitted SED obtained by attenuating the HE0238 SED by the very high-phase solution of S2. The VHH SED in green is the transmitted SED obtained by having the HE0238 SED attenuated first by the very high phase and then by the high phase. Right panel: the H SED (in red) was obtained by attenuating the HE0238 SED by the high-phase solution of S2. The HVH SED in dark green is the transmitted SED obtained by having the HE0238 SED attenuated first by the high phase and then by the very high phase.

6.3. Volume Filling Factor and S2 Velocity Shift

From Equation (6) in Paper II, the volume filling factor for two phases is given by

$$f_V = \frac{U_{H,HP}}{U_{H,VHP}} \times \frac{N_{H,HP}}{N_{H,VHP}}, \quad (6)$$

where HP and VHP denote the high phase and very high phase, respectively (see also Section 2.5 in Paper I). S1 and S2 have f_V values of 8×10^{-3} and 4×10^{-3} , respectively (see Table 5). These values are similar to those in Papers II, III, IV, and VI but are 3–4 orders of magnitude larger than what is seen in HE0238-1904 (Arav et al. 2013).

Given the ionization potential-dependent velocity shift between the troughs in S2, it warrants a closer look at the properties of S2. The very high phase has a thickness of $\Delta R = N_H/n_e = 2 \times 10^{-3}$ pc while the high phase has $\Delta R = 8 \times 10^{-6}$ pc. The densities are also among the highest that have been measured to date. Therefore, it is possible that these high densities and thicknesses are related to the observed velocity shift. Paper II also shows an outflow (in SDSS J1042+1646 at -7500 km s $^{-1}$) with the same very high-phase n_e as S2 and an n_e for the high phase that is half that of the high-phase n_e for S2. Both phases in the SDSS J1042+1646 outflow also have larger thicknesses by about five times that of the corresponding phases of S2. However, a velocity shift analysis could not be done for that outflow since the only observed high-ionization potential ions were O IV and N IV, and the troughs were blended and wide, making velocity centroid measurements unreliable.

6.4. X-Ray Warm Absorber Connection

X-ray warm absorbers have been shown to span up to 5 orders of magnitude in the ionization parameter, i.e., $-1 < \log(\xi) < 4$ (for the HE0238 SED, $\log(\xi) \approx \log(U_H) + 1.3$), and a continuous N_H as a function of ξ is often invoked (e.g., Steenbrugge et al. 2003; Costantini et al. 2007; Holczer et al. 2007; McKernan et al. 2007; Behar 2009). The necessity of the two phases to sufficiently explain the observed absorption troughs from the high and very high-ionization potential ions in

PKS J0352-0711 is similar to what is seen for X-ray warm absorbers, and we can not rule out phases at higher U_H and N_H with our data. The U_H and N_H are also comparable to those determined for X-ray warm absorbers. Current X-ray observatories (*XMM-Newton* and *Chandra*) do not have the sensitivity to obtain useful data on outflows in luminous quasars like PKS J0352-0711. However, the future observatory Athena (Barcons et al. 2017) is designed to have over 50 times the effective area (at 1 keV) for spectroscopy compared to current observatories, enabling more distant quasars to be probed.

6.5. The S2 Outflow “Shading Effect” on the S1 Outflow

Since S2 at 9 pc is interior to S1 at 500 pc, the SED seen by S1 will likely be attenuated by S2 (e.g., Bautista et al. 2010; Sun et al. 2017; Miller et al. 2018). To test the effects this may have on the results of S1, we followed the procedure outlined in Miller et al. (2018). We first generated new grids of Cloudy models using the transmitted SEDs from the high and very high photoionization solutions for S2 as well as the combination of the two (See Figure 9 for a comparison of each SED with the HE0238 SED). From these grids, new photoionization solutions and energetics were determined. For the shading from both the high phase (H SED) and very high phase (VH SED), R , \dot{M} , and \dot{E}_K decreased by less than 30%. The SEDs obtained by having the HE0238 SED attenuated first by the very high phase and then by the high phase (VHH SED) and vice versa (HVH SED) decreased R , \dot{M} , and \dot{E}_K by about 50%. These effects are small for the energetics, but the change in the distance is comparable to the error. However, the main conclusion that S1 is not contributing to major AGN feedback remains unchanged.

7. Summary and Conclusions

In this paper, we presented *HST*/COS spectra for the quasar outflows seen in PKS J0352-0711. For the first time, we identified absorption troughs from ions Ca IV–V, Ca V*, and Ca VII*–VIII*. From the absorption troughs, ionic column densities for both outflow systems were calculated. A grid of photoionization models in conjunction with the ionic column

densities enabled the determination of the best-fit solutions for U_{H} and N_{H} of each outflow system.

The absorption troughs from O V*, Ca VII*, and Ca VIII* in S2 and O IV and O IV* in S1 yielded reliable density sensitive ratios. The O V* column density ratio provided the S2 very high-phase n_{e} , and the Ca VII* and Ca VIII* column density ratios independently confirmed the O V* derived n_{e} . The O IV density ratio yielded the S1 high-phase n_{e} . From these electron number densities, the distance to the central source of each outflow was calculated with Equation (3). Equations (4) and (5), along with the distance, enabled the determination of the mass flux and kinetic luminosity. Finally, the likely insignificant contribution each outflow has to AGN feedback processes was assessed, and these results were summarized in Table 5.

The following emerges from this work:

1. The extreme UV *HST*/COS observations revealed never-before-seen absorption troughs with those from Ca VII* and Ca VIII* being the most important. Their discoveries independently confirmed the O V*—derived electron number density, distance, and energetics of S2.
2. Both outflow systems required a two-phase ionization solution, just like HE0238-1904, to satisfy the column density measurements of both the very high-ionization potential and high-ionization potential ions observed in each system.
3. The very high-ionization potential ions and the large associated hydrogen column density are similar to what is seen in the X-ray warm absorbers.

T.M., N.A., and X.X. acknowledge support from NASA grants *HST* GO 14777, 14242, 14054, and 14176. This support is provided by NASA through a grant from the Space Telescope Science Institute, which is operated by the Association of Universities for Research in Astronomy, Incorporated, under NASA contract NAS5-26555. T.M. and N.A. also acknowledge support from NASA ADAP 48020 and NSF grant AST 1413319. CHIANTI is a collaborative project involving George Mason University (USA), the University of Michigan (USA), and the University of Cambridge (UK).

ORCID iDs

Timothy R. Miller  <https://orcid.org/0000-0002-0730-2322>

Nahum Arav  <https://orcid.org/0000-0003-2991-4618>

Xinfeng Xu  <https://orcid.org/0000-0002-9217-7051>

Gerard A. Kriss  <https://orcid.org/0000-0002-2180-8266>

References

- Anders, E., & Grevesse, N. 1989, *GeCoA*, **53**, 197
- Arav, N., Gabel, J. R., Korista, K. T., et al. 2007, *ApJ*, **658**, 829
- Arav, N., Borguet, B., Chamberlain, C., Edmonds, D., & Danforth, C. 2013, *MNRAS*, **436**, 3286
- Arav, N., Chamberlain, C., Kriss, G. A., et al. 2015, *A&A*, **577**, A37
- Arav, N., Liu, G., Xu, X., et al. 2018, *ApJ*, **857**, 60
- Arav, N., Xu, X., Miller, T., Kriss, G. A., & Plesha, R. 2020, *ApJS*, **247**, 37
- Arnett, D. 1996, *Supernovae and Nucleosynthesis: An Investigation of the History of Matter, from the Big Bang to the Present* (Princeton, NJ: Princeton Univ. Press)
- Bahk, H., Woo, J.-H., & Park, D. 2019, *ApJ*, **875**, 50
- Ballerio, S. K., Matteucci, F., Ciotti, L., et al. 2008, *A&A*, **478**, 335
- Barcons, X., Barret, D., Decourchelle, A., et al. 2017, *AN*, **338**, 153
- Bautista, M. A., Dunn, J. P., Arav, N., et al. 2010, *ApJ*, **713**, 25
- Bechtold, J., Dobrzycki, A., Wilden, B., et al. 2002, *ApJS*, **140**, 143
- Behar, E. 2009, *ApJ*, **703**, 1346
- Borguet, B. C. J., Edmonds, D., Arav, N., Dunn, J., & Kriss, G. A. 2012a, *ApJ*, **751**, 107
- Borguet, B. C. J., Edmonds, D., Arav, N., Benn, C., & Chamberlain, C. 2012b, *ApJ*, **758**, 69
- Chamberlain, C., & Arav, N. 2015, *MNRAS*, **454**, 675
- Costantini, E., Kaastra, J. S., Arav, N., et al. 2007, *A&A*, **461**, 121
- Crenshaw, D. M., Kraemer, S. B., & George, I. M. 2003, *ARA&A*, **41**, 117
- Dai, X., Shankar, F., & Sivakoff, G. R. 2008, *ApJ*, **672**, 108
- de Kool, M., Arav, N., Becker, R. H., et al. 2001, *ApJ*, **548**, 609
- de Kool, M., Becker, R. H., Arav, N., Gregg, M. D., & White, R. L. 2002, *ApJ*, **570**, 514
- Dere, K. P., Landi, E., Mason, H. E., Monsignori, B. C., & Young, P. R. 1997, *A&AS*, **125**, 149
- Dunn, J. P., Bautista, M., Arav, N., et al. 2010, *ApJ*, **709**, 611
- Ferland, G. J., Chatzikos, M., Guzmán, F., et al. 2017, *RMxAA*, **53**, 385
- Finn, C. W., Morris, S. L., Crighton, N. H. M., et al. 2014, *MNRAS*, **440**, 3317
- Gabel, J. R., Arav, N., & Kim, T.-S. 2006, *ApJ*, **646**, 742
- Ganguly, R., & Brotherton, M. S. 2008, *ApJ*, **672**, 102
- Green, J. C., Froning, C. S., Osterman, S., et al. 2012, *ApJ*, **744**, 60
- Grevesse, N., Asplund, M., Sauval, A. J., & Scott, P. 2010, *Ap&SS*, **328**, 179
- Hamann, F., & Ferland, G. 1993, *ApJ*, **418**, 11
- Hamann, F. W., Barlow, T. A., Chaffee, F. C., Foltz, C. B., & Weymann, R. J. 2001, *ApJ*, **550**, 142
- Hewett, P. C., & Foltz, C. B. 2003, *AJ*, **125**, 1784
- Holczer, T., Behar, E., & Kaspi, S. 2007, *ApJ*, **663**, 799
- Hopkins, P. F., & Elvis, M. 2010, *MNRAS*, **401**, 7
- Kaastra, J. S., Mewe, R., Liedahl, D. A., et al. 2000, *A&A*, **354**, L83
- Kaastra, J. S., Kriss, G. A., Cappi, M., et al. 2014, *Sci*, **345**, 64
- Knigge, C., Scaringi, S., Goad, M. R., & Cottis, C. E. 2008, *MNRAS*, **386**, 1426
- Korista, K. T., Bautista, M. A., Arav, N., et al. 2008, *ApJ*, **688**, 108
- Landi, E., Young, P. R., Dere, K. P., Del Zanna, G., & Mason, H. E. 2013, *ApJ*, **763**, 86
- Mathews, W. G., & Ferland, G. J. 1987, *ApJ*, **323**, 456
- McKernan, B., Yaqoob, T., & Reynolds, C. S. 2007, *MNRAS*, **379**, 1359
- Miller, T. R., Arav, N., Xu, X., et al. 2018, *ApJ*, **865**, 90
- Miller, T. R., Arav, N., Xu, X., Kriss, G. A., & Plesha, R. 2020, *ApJS*, **247**, 39
- Murray, N., Chiang, J., Grossman, S. A., & Voit, G. M. 1995, *ApJ*, **451**, 498
- Muzahid, S., Srianand, R., Arav, N., et al. 2013, *MNRAS*, **431**, 2885
- Proga, D., Stone, J. M., & Kallman, T. R. 2000, *ApJ*, **543**, 686
- Proga, D., & Kallman, T. R. 2004, *ApJ*, **616**, 688
- Reynolds, C. S. 1997, *MNRAS*, **286**, 513
- Scannapieco, E., & Oh, S. P. 2004, *ApJ*, **608**, 62
- Schlaflly, E. F., & Finkbeiner, D. P. 2011, *ApJ*, **737**, 103
- Steenbrugge, K. C., Kaastra, J. S., de Vries, C. P., et al. 2003, *A&A*, **402**, 477
- Sun, L., Zhou, H., Ji, T., et al. 2017, *ApJ*, **838**, 88
- Wright, E. L. 2006, *PASP*, **118**, 1711
- Xu, X., Arav, N., Miller, T., & Benn, C. 2018, *ApJ*, **858**, 39
- Xu, X., Arav, N., Miller, T., et al. 2019, *ApJ*, **876**, 105
- Xu, X., Arav, N., Miller, T., Kriss, G. A., & Plesha, R. 2020a, *ApJS*, **247**, 38
- Xu, X., Arav, N., Miller, T., Kriss, G. A., & Plesha, R. 2020b, *ApJS*, **247**, 40
- Xu, X., Arav, N., Miller, T., Kriss, G. A., & Plesha, R. 2020c, *ApJS*, **247**, 42